Carbon Trends 5 (2021) 100097

Contents lists available at ScienceDirect

Carbon Trends

journal homepage: www.elsevier.com/locate/cartre

Loading dependency of 2D MoS_2 nanosheets in the capacitance of 3D hybrid microfibre-based energy storage devices

Anup K Roy[a,*], Shaikh N Faisal[a,b], Axel Spickenheuer[c], Christina Scheffler[c], Jiawei Wang[d], Andrew T Harris[a], Andrew I Minett[a], Mohammad S Islam[d,e,*]

[a] Laboratory for Sustainable Technology, School of Chemical and Biomolecular Engineering, The University of Sydney, Sydney NSW 2006, Australia
[b] School of Electrical and Data Engineering, University of Technology Sydney, Sydney, NSW 2007, Australia
[c] Leibniz-Institute für Polymerforschung Dresden e. V., Hohe Str. 6, Dresden 01069, Germany
[d] Mechanical and Manufacturing Engineering, The University of New South Wales, Sydney, NSW 2052, Australia
[e] School of Aerospace, Mechanical and Mechatronic Engineering, The University of Sydney, Sydney, NSW 2006, Australia

ARTICLE INFO

Article history:
Received 1 June 2021
Revised 16 August 2021
Accepted 17 August 2021

Keywords:
Multifunctional hybrid composite fibre
Liquid-crystal
Textile supercapacitors
Mechanical properties
Molybdenum disulphide

ABSTRACT

This study reports a wet spinning method to spin composite micro-fibres of 2D liquid crystalline graphene oxide (GO) and exfoliated MoS_2 nanosheets with very high MoS_2 loading. The MoS_2 dispersion was found to be isotropic irrespective of solvent type or solute concentration in the dispersion and thus found to be non-spinnable via wet spinning process. The liquid crystallinity of GO induces birefringence in the composite dispersion and enables the spinning of the composite dispersion containing high loading of MoS_2 with great flexibility. We were able to spin composite microfibers with 69 wt% MoS_2 loading for the first time. The resulting fibres were annealed at high temperature to produce flexible conductive rGO#MoS_2 fibres. Scanning electron microscopy (SEM) and Raman analysis strongly suggest homogeneous distribution of MoS_2 throughout the fibres. Mechanical properties of the fibres were studied and maximum tensile strength (76.5 MPa) and Young's modulus (13.3 GPa) obtained with 10 wt% MoS_2 loading. All solid-state flexible symmetric supercapacitor from these composite fibres was fabricated and the electrochemical performance was studied. The electrochemical study shows high areal capacitance of the produced composite fibres (as high as 282.6 mF cm^{-2}) with good cycling stability (82.5% capacitance retention after 5000 cycles) that indicates high potential of these composite fibres as energy storage system for smart textile of the future.

1. Introduction

With the invention of smart technologies for sensors and devices, it is not very far that the very cloth we wear everyday will become smart fabric with incorporated sensors and devices. These sensors and devices can continuously monitor our vital life sign to maintain our basic bodily functions regularly to protect us better [1–6]. To make this fabric smart, it will need to have incorporated energy sources to provide enough power to run throughout the day. Nanomaterial based advanced fibre technology will pave the pathway in fulfilling the immense potential this technology holds owing to its high flexibility, knittability and wearability [7,8]. Number of studies have been published in recent years that reports fibre based supercapacitors [9–11], sensors [12,13], actuators [14,15], solar-cells [16–18], and batteries [8,19] that could be impregnated into smart textiles.

2D Graphene have attracted intense research interest in past decade due to its superior mechanical, electrical, chemical and optical properties [20–26] . Many studies have been carried out on making graphene yarn for the textile application [27–30]. These fibres have shown to incorporate good mechanical strength and performance. However, graphene fibre-based energy storage devices suffer from comparatively lower capacitance then planer electrodes as well as stacking tendency of graphene layers in the fibre electrodes [11,31,32]. In recent years, liquid crystal graphene oxide has gained a lot of attention as a precursor for graphene as it can be processed into films and continuous fibres with ease [29,33]. The final architecture possesses high unidirectional properties as well as excellent flexibility. In recent years, many researches have reported a simple wet spinning method to produce continuous GO

* Corresponding author.
E-mail addresses: anup.roy@sydney.edu.au (A.K. Roy), m.s.islam@unsw.edu.au (M.S. Islam).

https://doi.org/10.1016/j.cartre.2021.100097

fibres from aqueous liquid crystal (LC)-GO dispersions with high degree of alignment and excellent mechanical properties [34,35]. These fibres can further be treated via chemical or thermal reduction to produce reduced GO (rGO) fibres that closely resembles the properties of graphene [36]. This process is advantageous in many aspects compared to the widely used energy intensive spinning process to produce carbon fibres commercially.

Besides graphene, the most studied 2D material belongs to the group known as transition metal dichalcogenides (TMDs) [37–39]. TMDs possess wide variety of physical, electrical and mechanical properties that can be efficiently utilized to produce high performance fibre electrodes. Compositing graphene/graphene oxide with TMDs could be an effective solution for overcoming the challenges related to graphene fibres as it can combine the excellent properties of graphene and TMDs in one single fibre while compensating for their shortcomings [11]. Graphene will provide the conductive network and backbone of the fibre while TMDs can be utilized to impart the desired properties on the fibre. Also, they will act as nano-spacers if intercalated effectively and thus prevent stacking of graphene layers. Several studies have reported graphene TMD based composite fibres that were utilized in textile applications. The first reported graphene-TMD based fibre was by Sun et al. [9] which involved simple wet spinning process to fabricate ultra-long hybrid microfibers of GO with TMDs (MoS_2, TiS_2, TaS_2 etc.).MoS_2 is the most researched TMD for various applications such as coating, electrocatalysis and supercapacitors [40–43]. However, in terms of fibre manufacture, the reported achievable MoS_2 loading was only up to 2.2 wt% above which the fibres disintegrate in the spinning bath [10,11,44–46]. The highest achievable loading of MoS_2 on a hybrid fibre was found to be about 34 wt% reported by Wang et al. [11]. They adopted a hydrothermal method to form graphene/MoS_2 hybrid fibres inside a sealed polytetrafluoroethylene (PTFE) tube (ID 0.5 mm). The result showed good mechanical properties with improved charge storage capacity to be used as textile capacitor. The limitation in the method, however, was the continuous formation of fibres as the fibre length was limited by the length of the PTFE tube used. Besides that, higher loading of MoS_2 beyond 34 wt% was not achievable.

Herein, we demonstrate a simple wet spinning strategy to produce hybrid microfibres of graphene oxide and MoS_2 with very high MoS_2 loading. The mesophase ordering of GO in dispersion dictates the binder free spinning of fibres. It also has shown to induce LC-like ordering in isotropic MoS_2 dispersion and thus enables spinning of GO-MoS_2 fibres without the necessity of polymeric binders. A range of GO-MoS_2 composite fibres were prepared where the MoS_2 loading were varied from 5 to 70 wt%. To the best of our knowledge, such high loading of MoS_2 has never been achieved. The fibres were extensively characterized and finally as a proof-of-concept application, flexible, solid-state two electrode supercapacitor devices were fabricated using these hybrid fibres and their performance was studied. The efficient intercalation technique produces high performance fibre electrodes that can not only be used for supercapacitor application but can be utilized for many other potential applications.

2. Experimental

2.1. Synthesis of GO

Liquid crystal dispersion of graphene oxide (GO) was prepared using a modified Hummers method [33,35,47]. Acid-intercalated natural graphite was thermally expanded at 1050°C for 5s to make thermally expanded graphite. This expanded graphite was used to produce the GO sheets using the Hummers process which were then redispersed with deionised (DI) water with GO concentration of 10.0 mg/ml.

2.2. Exfoliation of MoS_2

Bulk MoS_2 was exfoliated using probe sonication. 1.0 g of MoS_2 powder (Sigma Aldrich, Average particle size $\approx$ 6.0 μm) was dispersed in DI water using 0.3 g of sodium cholate surfactant. For liquid exfoliation technique, sodium cholate acts as ionic surfactant to keep the graphene flakes apart in solution and thus prevent agglomeration [48]. The mixture was then sonicated with a probe sonicator (60% of 400 W with 40% duty cycle) for 4.0 h in an ice bath. Afterward the resulting mixture was centrifuged at 1000 rpm for 1 h and the supernatant was collected and used for further experiments.

2.3. Fabrication of composite fibres

GO and MoS_2 dispersions were mixed in different mass ratios using a vortex mixer for 10 min to produce hybrid dispersions of different weight loadings of MoS_2. The dispersions were then centrifuged and rinsed with DI water for few times to remove sodium cholate from it. Finally, the precipitates were redispersed in DI water using a vortex mixer. These hybrid mixtures were then used to spin composite fibres with an overall GO concentration of 5.0 mg ml^{-1}. For the wet spinning process, a solution of 10 wt% $CaCl_2$ in 50:50 (v/v) mixture of water and ethanol was used. In a typical spinning process, the composite dispersion was injected in a rotating bath (20 rpm) of coagulant at a flow rate of 20 ml h^{-1} using a syringe pump. The schematic of the process is presented in Fig. S1. The fibres were formed immediately in the bath and then left in the bath for an hour before washing with ethanol to remove $CaCl_2$ salt. The fibres were then collected from the bath after 24 h and dried overnight in tension at room temperature.

2.4. Reduction of the fibres

To improve the conductivity of both, GO and GO#MoS_2 composite fibres, they were reduced in a similar manner to remove functional oxide groups. To achieve that the fibres were mounted on ceramic crucible and annealed at 400 °C for 1 h with N_2 (flow rate 300 SCCM) to produce r-GO and r-GO#MoS_2 fibres. Besides reducing the surface functional group, the annealing process also increase nanocrystallinity in MoS_2 that can enhance the overall electrochemical properties [34, 49].

2.5. Mechanical testing of the composite fibres

The tensile properties of both neat GO and GO#MoS_2 composite single fibres were determined using a dynamic mechanical analyzer (DMA) (TA Instrument DMA 2980). Single fibres were attached to paper windows of 30 $\times$ 10 mm size with 10 mm holes punched into them to give a gauge length of 10 mm. Polyvinyl acetate (PVA) glue was used to hold the fibres in place on the paper window. The fibres were then placed under an optical microscope and inspected with a calibrated eyepiece (200x magnification) to determine the average diameter of each of the fibres. The paper window was then placed into the grips of the DMA tensile clamp, and the sides of the paper window were cut, leaving only the single fibre between the grips. Single fibre tensile tests with at least 10 replicates per sample were conducted using a DMA with a crosshead speed of 0.5 mm/min. All the tests were performed at 25 °C with a preload force of 0.001 N.

2.6. Characterization

Individual GO sheets and MoS_2 nano sheets were examined using a Zeiss Ultra Plus Field Emission Scanning Electron Microscope (FESEM). The nanosheets were deposited onto silanized silicon wafer. Silanization was carried out using a pre-cleaned silicon

wafer into 3-aminopropyltriethoxysilane (Sigma–Aldrich) in water (1:9 v/v) with one drop of hydrochloric acid (Sigma–Aldrich) for 30 min. The nanosheets were then deposited by immersing the silanized silicon wafer into 5 μg ml^{-1} dispersions of GO or MoS_2 dispersions for 5 s followed by washing with DI water. The morphology of GO and hybrid fibres was also investigated using the FESEM. Prior to SEM, the non-conducting fibres were first sputter coated with 15 nm of Au for better resolution. The birefringence of GO and GO#MoS_2 hybrid dispersions was studied using a Leica CTR 6000 polarised optical microscope (POM) operated in transmission mode. For sample preparation, 200 μL of the dispersion was placed in a glass slide and covered with a cover slip. The Raman spectra were measured using a Renishaw microRaman spectroscopy system with a 514.5 nm argon-ion laser under ambient conditions. To confirm the consistency of the results, scans were taken at various spots of each individual film. X-ray photoelectron spectroscopy (XPS) analysis was carried out using an instrument (ESCALAB250Xi) with mono-chromated Al K alpha (energy 1486.68 eV) X-ray source of radiation at 90° electron take-off angle. TGA analysis was performed using a Netzsch TG209 Tarsus DTA-TGA from RT to 700°C at a heating rate of 20°C min^{-1} under an Air environment.

2.7. Electrochemical characterization

The two-electrode configuration was tested using cyclic voltammetry and galvanostatic charge discharge in H_2SO_4-PVA based polymer gel electrolyte. Well defined CV curves were observed within the potential window of 0.0 to -0.8 V. The working electrode was constructed using 2 pieces of fibre of about 51 µm diameter. The volumetric specific capacitance C_{vol} of all the devices were calculated from the galvanostatic charge discharge curves according to the following equation [50].

$$C_{vol} = \frac{4I}{v(dV/dt)} \tag{1}$$

where, I (A) is the discharge current, v is the total volume of the fibres in the device that is exposed to the electrolyte, dV (V) is the potential window and dt (s) is the discharge time.

The energy density, E and power density, P of the devices were calculated according to Eqs. 2 and 3, respectively, as shown below:

$$E = \frac{C_{vol}V_{max}^2}{2} \tag{2}$$

$$P = \frac{E}{dt} \tag{3}$$

where, $V_{\max}$ is the maximum operating voltage of the discharge curve.

3. Results and discussion

Liquid crystalline dispersion of graphene oxide (GO) was prepared using a modified Hummers method. Fig. 1(a) shows the scanning electron microscopic (SEM) image of the as synthesized GO sheets mounted on silanized Si-wafer. Large monolayer GO sheets with wrinkled appearance can be seen with average/lateral sheet size ranges from 50 μm – 80 μm. These high aspect-ratio GO sheets facilitates the formulation of nematic liquid crystals of GO in aqueous medium [33, 34].

The isotropic to nematic phase transformation (liquid crystallinity) of GO in aqueous medium is a concentration dependent property [35]. We studied the isotopic to nematic phase transformation of aqueous GO dispersions with concentration by observing their birefringence under polarized light using an optical microscope with cross polarizer. The result showed a visible phase transformation from isotropic to nematic above GO concentration of 0.5 mg ml^{-1} to a concentration of 2.0 mg ml^{-1} and above this concentration range the dispersion displays complete nematic behaviour. The inset of Fig. 1(a) shows an image of GO dispersion (1 mg ml^{-1}) in glass vial under polarized light. It shows a pattern that is typical of a nematic liquid crystal [34, 51]. Fig. S2(a) represents the polarized optical microscopy image of GO dispersion of 5.0 mg ml^{-1} concentration which exhibits full nematic phase texture under cross polarizer. This advantageous LC property has enabled the spinning of GO into fibres without the addition of any sort of polymeric binders to hold the GO sheets together [33]. Raman is a widely used non-destructive characterization technique that was used to study the GO further. The Raman spectra of LC-GO shown in Fig. 1(b) consists of two characteristic peaks observed at 1350 cm^{-1} and 1602 cm^{-1} corresponding to D and G band, respectively. The G band is ascribed to the in-plane vibration of sp^2 carbon atoms, while the D band is attributed to breathing modes of six-atom rings and requires a defect for its activation. The I_D/I_G ratio used as an index for GO and graphene quality was found to be 0.93 for the LC-GO.

Aqueous dispersion of layered MoS_2 was prepared by exfoliation of bulk MoS_2 particles (Sigma Aldrich, mean size > 6 μm) in aqueous medium using a probe sonicator. Upon sonication, the stacked multilayer MoS_2 particles are exfoliated to a few layer nanosheets with the size range of a few hundred nanometres. Fig. 2(a) shows the exfoliated MoS_2 dispersions of different concentrations. The degree of exfoliation was investigated using TEM and HRTEM as shown in Fig. 2(b–d). It is evident from the figure that the bulk particles had exfoliated to a certain degree to form 2D nanosheets with a fewer layer and a few hundred nanometres of size.

To further inspect the degree of exfoliation, RAMAN analysis was also performed which can provide vital information about material exfoliation. Fig. 2(e) shows Raman spectrum for bulk and exfoliated MoS_2. Well-defined peaks within the range of 350 cm^{-1} – 450 cm^{-1} were observed which are indicative peaks of MoS_2. A shift in peaks was observed towards the right for the sonicated dispersion, which is believed to be due to the exfoliation of the bulk particles to a fewer layer.

Formation of liquid crystalline in aqueous dispersion enables the formation of novel self-assembled 3D architectures. The as synthesized surfactant stabilized exfoliated MoS_2 dispersion is isotropic regardless of the size and concentration of MoS_2. Fig. S2(b) shows the POM images of aqueous exfoliated MoS_2 dispersion, which indicates the isotropic nature of the dispersion. To rule out the concentration effect, the POM images were taken at higher concentrations, but no visible change was observed.

It is therefore not possible to spin fibres from MoS_2 dispersion irrespective of the concentration of the dispersion. For being able to spin fibres, we either have to add polymer binder that can hold the individual particles of MoS_2 together to form continuous microfibre architecture or have to transform the isotropic MoS_2 dispersion to nematic phase (induce liquid crystallinity). Herein, we took the second route and inspect the outcomes of inducing liquid crystallinity in isotropic MoS_2 dispersion by adding aqueous LC-GO dispersion in it. LC-GO and MoS_2 dispersions were mixed in exact proportion to maintain the final concentration of GO in the mixture to be 5.0 mg ml^{-1}. Thus, we can rule out the possibility of the dispersion not being liquid crystalline due to the final concentration of GO falls below the level where GO does not exhibit liquid crystallinity.

The effect of addition of LC-GO into MoS_2 dispersion was observed using an optical microscope with a cross polarizer as shown in Fig. S2(c). It is evident from the micrographs that with addition of LC-GO into the MoS_2 dispersion it transforms from isotropic to nematic dispersion. The lyotropic LC formation in aqueous disper-

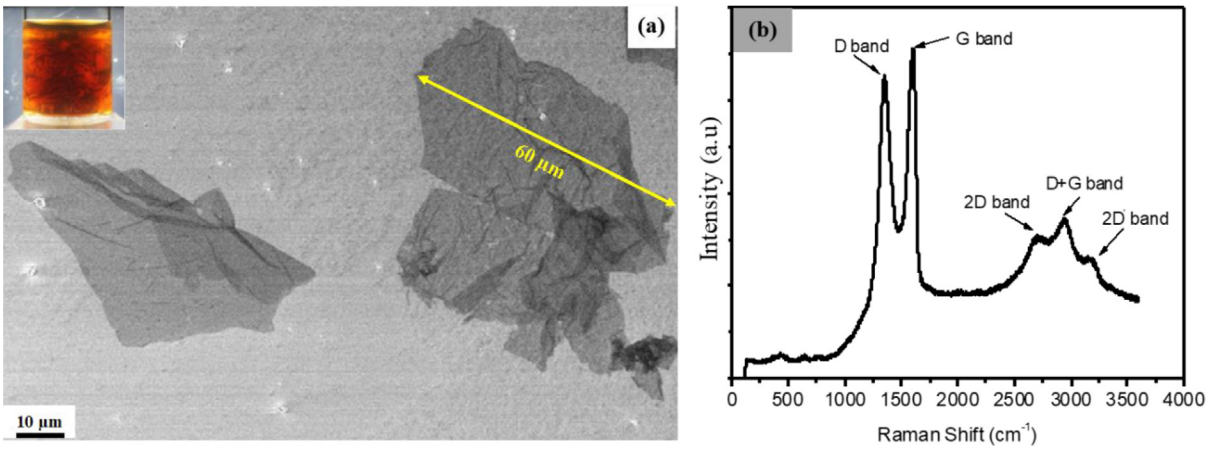

Fig. 1. (a) SEM micrographs of GO nanosheets mounted on a pre-silanized silicon wafer. Inset shows the image of a GO dispersion under polarized light, and (b) Raman spectrum of GO.

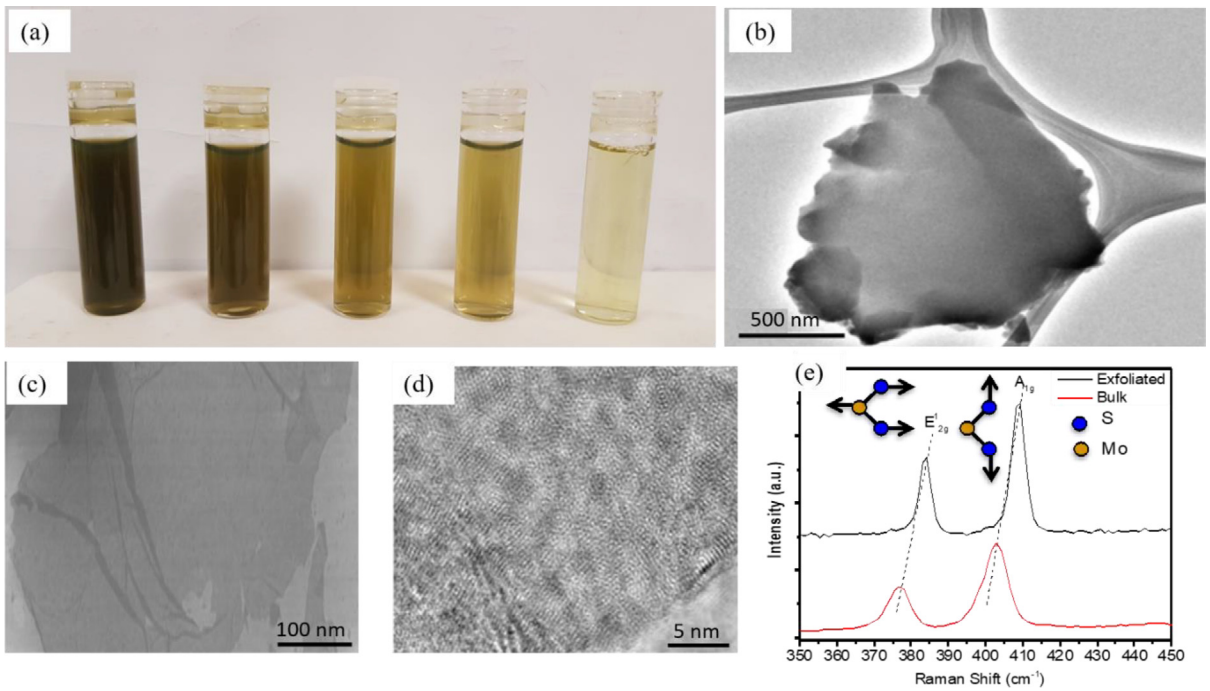

Fig. 2. (a) Image showing exfoliated MoS_2 dispersion at different concentrations with the concentration decreasing from left to right, (b) TEM image of an exfoliated MoS_2 particle mounted in a copper grid, (c) TEM and (d) HRTEM image of exfoliated MoS_2 nanosheets, and (e) Raman spectrum of bulk and exfoliated MoS_2.

sions was well studied by Jalili *et al.* and described as an entropy-driven process [35, 52]. Two types of entropy, namely orientational entropy and positional entropy plays the key role in isotropic-nematic transition in dispersion. We extend their findings relating to the formation of LC phase in aqueous GO dispersion to explain the isotropic to nematic phase transformation in our composite dispersions and their spinnability. The addition of ultra large GO sheets into a dispersion of small MoS_2 nanosheets produces a polydispersed colloidal suspension. The larger GO sheets create the excluded volume for smaller MoS_2 sheets and thus impart long range LC like ordering to show birefringence under polarized light. This excluded volume effect induces entropic rearrangement giving rise to positional entropy and reduction of orientational entropy, which governs the formation of LC phase in the composite [35, 47].

The crystal-like ordering of MoS_2 layers induced by the addition of adequate amount of large GO sheets in dispersion allows us to fabricate composite microfibres of GO#MoS_2 with high loading of MoS_2 in the composite in a simple wet spinning process without the need of using polymer binder. We fabricated wet spun microfibres from the GO#MoS_2 composite dispersions with MoS_2 loading ranging from 5 % to 70 % in the fibre. A composite microfiber with MoS_2 loading as high as 69 % has been prepared which was never achieved before. A further increase in weight loading of MoS_2 was not possible as the fibre tends to disintegrate easily in the coagulation bath.

One big advantage of the wet spinning process employed in this study is that it is scalable and can produce continuous fibre without any complex synthesis needed. The fibre formation here can be divided into two stages [34]. Firstly, when the LC dispersion is pumped through the spinneret needle, shear force is applied to the dispersion due to the high velocity flow in the needle capillary that induces alignment of the LC domains along the direction of the shear force [33,34,53]. When the dispersion goes into the coagulation bath, gelation of the stream begins instantaneously that causes the formation of an outer skin layer of GO sheets, and thus, forms the fibre-like architecture [34]. The Ca^{2+} ion in the coagu-

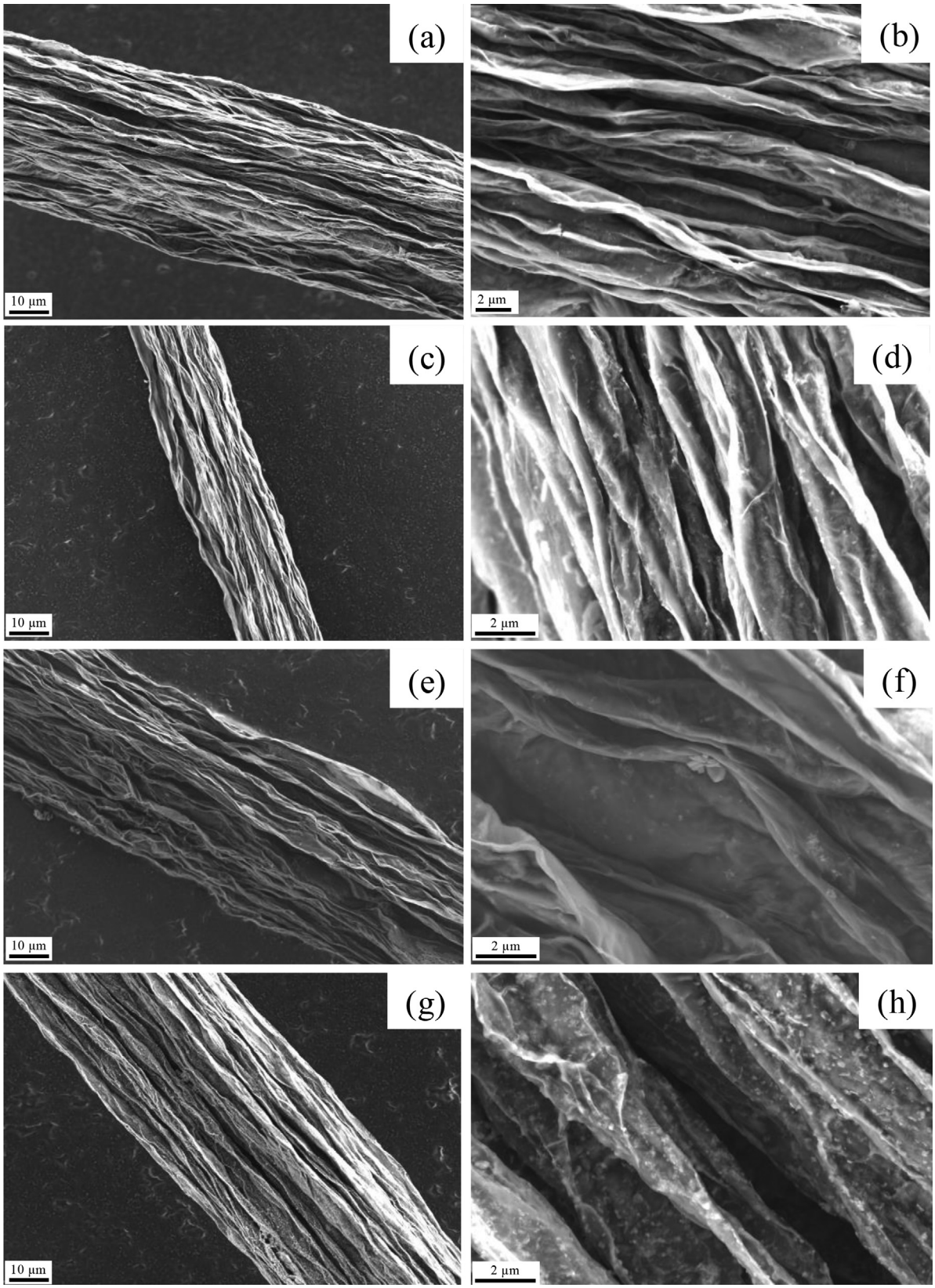

Fig. 3. FESEM image of (a-b) GO-MoS_2-5, (c,d) GO-MoS_2-10, (e,f) GO-MoS_2-20, and (g,h) GO-MoS_2-50 at low and high magnification, respectively.

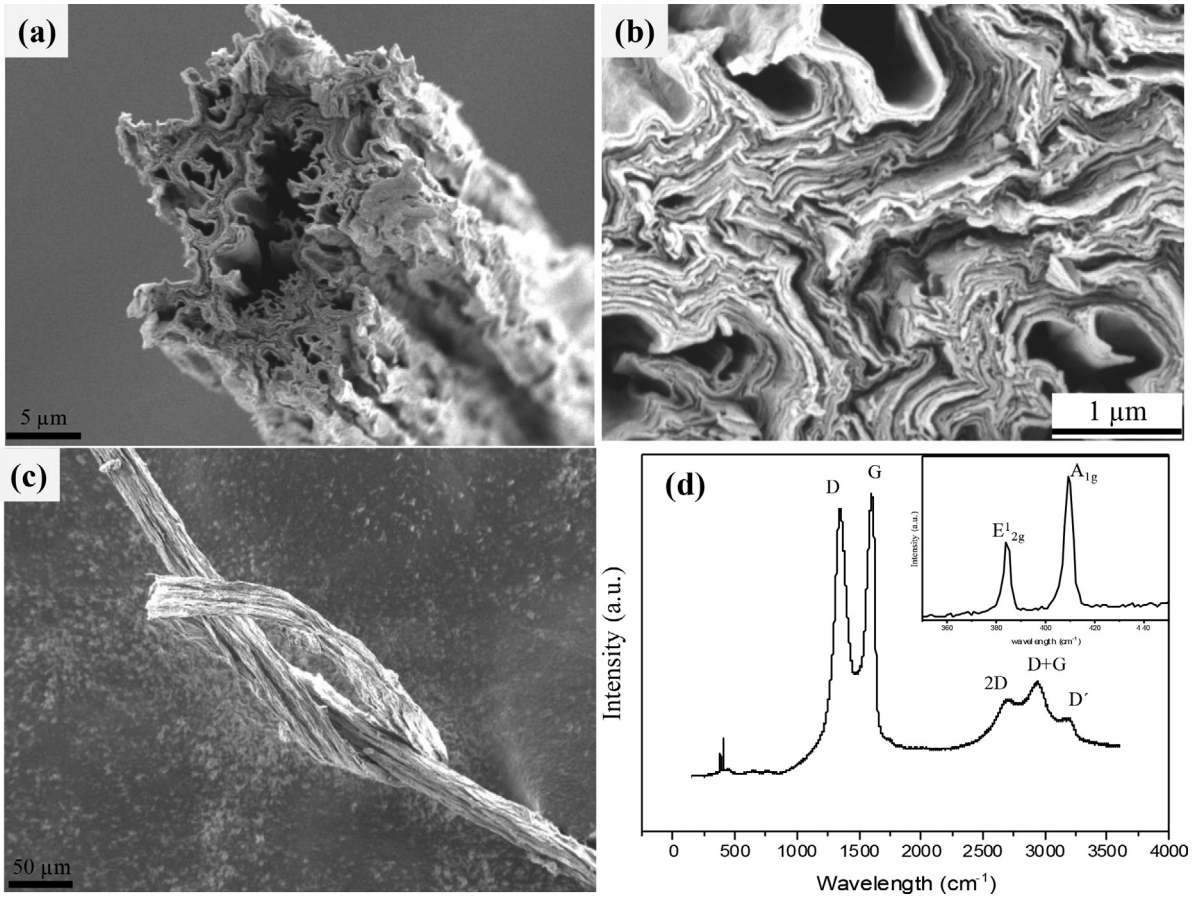

Fig. 4. (a) SEM image of the cross-section of a GO#MoS_2 composite fibre with 10 wt% MoS_2 loading, (b) Shows the higher magnification SEM of the same cross-section of (a), (c) SEM image of a knot tied with a GO#MoS_2 composite fibre (20% MoS_2), and (d) Raman spectra of a GO#MoS_2 composite fibre with 20 wt% MoS_2 loading (inset showing well-defined peaks within the range of 350–450 cm^{-1}).

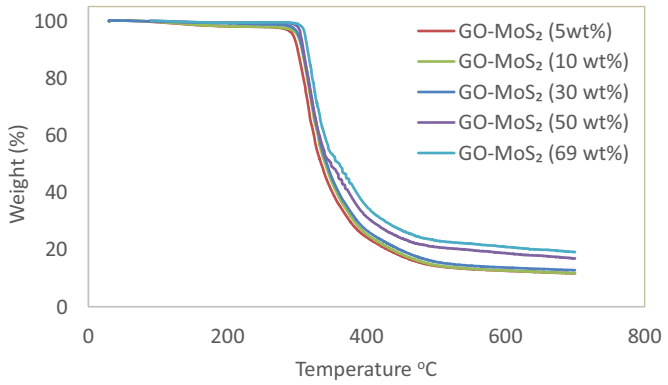

Fig. 5. TGA curves of GO-MoS_2 with different MoS_2 contents.

lation bath plays a vital role here. The diffusion of Ca^{2+} cations inside the fibre structure induces further cross-linking among individual GO sheets inside the structure, and thus, helps in solidification and improvement in mechanical properties. The second stage of the spinning process involves further alignment of the LC domain arises from the drawing force imparted on the fibre due to the difference between injection rate of the dispersion through the needle and the rpm of the coagulation bath. Too high of a drawing force will produce fibre of very short length. In contrast, low drawing force will produce lumps of LC-GO#MoS_2 in the spinneret nozzle and irregularity in the fibre shapes.

The morphology of both GO and the composite fibres was studied using SEM. Fig. S3 shows the representative SEM micrographs of GO fibre and its respective cross-section. Porous, non-circular geometry of highly aligned GO sheets are observed. Average fibre diameter was found to be within the range of 40 – 50 µm.

Due to the poor conductivity issue, to get better SEM micrographs, the GO#MoS_2 composite microfibres were annealed at 400°C for 1 hr in an inert environment (N_2 flow). The SEM images of the composite fibres are shown in Fig. 3. The morphology depicts the creation of highly porous, non-circular, crumpled microfibre with diameter in the range of 40–50 µm. A closer look into the porous fibre surface Fig. 3(b,d,f,h) reveals the uniform distribution of 2D MoS_2 nanosheets between individual layers of comparatively larger graphene oxide sheets. This uniform distribution was facilitated by the formation of LC phase in the composite dispersion that is believed to be dictated by LC-GO.

The cross-section of a composite fibre is shown in Fig. 4(a). It reveals the excellent alignment of the layered nanosheets that is not disrupted due to the addition of MoS_2 into LC-GO. This finding supports our claim of inducing liquid crystallinity onto MoS_2 by ordered domains of GO in solution.

The cross-section of the GO-MoS_2 fibres observed under SEM as shown in Fig. 4(b) reveals good alignment of GO sheets in the fibre. Even at very high loading of MoS_2, the fibres maintained an LC like ordering with high degree of orientation. To demonstrate the flexibility of the processed fibre obtained from the coagulation bath we tied multiple knots as demonstrated in Fig. 4(c). It is clear from the figure that the fibre shape was not distorted by the formation of a knot in the fibre. Further investigation on the distribution of MoS_2

Table 1
Performances of some recently reported graphene and MoS_2 based fibre supercapacitors.

Device configuration and cell voltage	Electrolyte	Capacitance	Energy and power density	Cycle life	Tensile properties			Refs.
					Strength (MPa)	Modulus (GPa)	Strain (%)	
Parallel and 1V (Fibre shaped rGO)	PVA-H_3PO_4	0.726 mF cm^{-2}	–	–	–	–	–	[36]
Parallel and 0.8V (rGO/Ni-Cotton yarn)	PVA/LiCl	–	6.1 mW h cm^{-3} and 1400 mW cm^{-3}	~82 % for 10000 cycles	53	–	8	[58]
Parallel and 1V (rGO coated carbon fibre)	PVA- H_3PO_4	307 mF cm^{-2}	0.0131 mW h cm^{-2} and 8.5 mW cm^{-2}	~85 % for 5000 cycles	–	–	–	[59]
Twisted and 1 V (rGO fibre)	PVA–H_2SO_4	1.7 mF cm^{-2}	1.7 10^{-4} mW h cm^{-2} and 0.01 mW cm^{-2}	–	145	–	0.95	[60]
Coaxial and 0.8 V (all core graphene fibre)	PVA– H_2SO_4	205 mF cm^{-2}	0.0175 mW h cm^{-2}	100 % for 10 000 cycles	–	–	–	[31]
All solid-state intertwined and 1.2 V (NaDC/GO/MoS_2 fibre)	PVA/H_3PO_4	332.8 mF cm^{-2}	32 mW h cm^{-3} and 1.18 W cm^{-3}	73 % (550 cycles)	204.3	–	13	[61]
All solid-state parallel and 1V (MoS_2/rGO/CNT hybrid fibre)	PVA/H_2SO_4	93.2 m Fcm^{-2}	26.4 Wh/Kg and 4000 W/Kg	85 % (5000 cycles)	88	–	1.4	[62]
Coaxial solid state and 0.8V (rGO/20 wt% MoS_2 fibre)	PVA- H_2SO_4	282.6 mF cm^{-2}	4.92 mW h cm^{-3} and 0.051 W cm^{-3}	87 % (1000 cycles)	37.3	5.8	0.95	Current study
Coaxial solid state and 0.8V (rGO/10 wt% MoS_2 fibre)	PVA- H_2SO_4	185.3 mF cm^{-2}	3.38 mW h cm^{-3} and 0.0936 W cm^{-3}	–	76.5	13.3	0.86	Current study

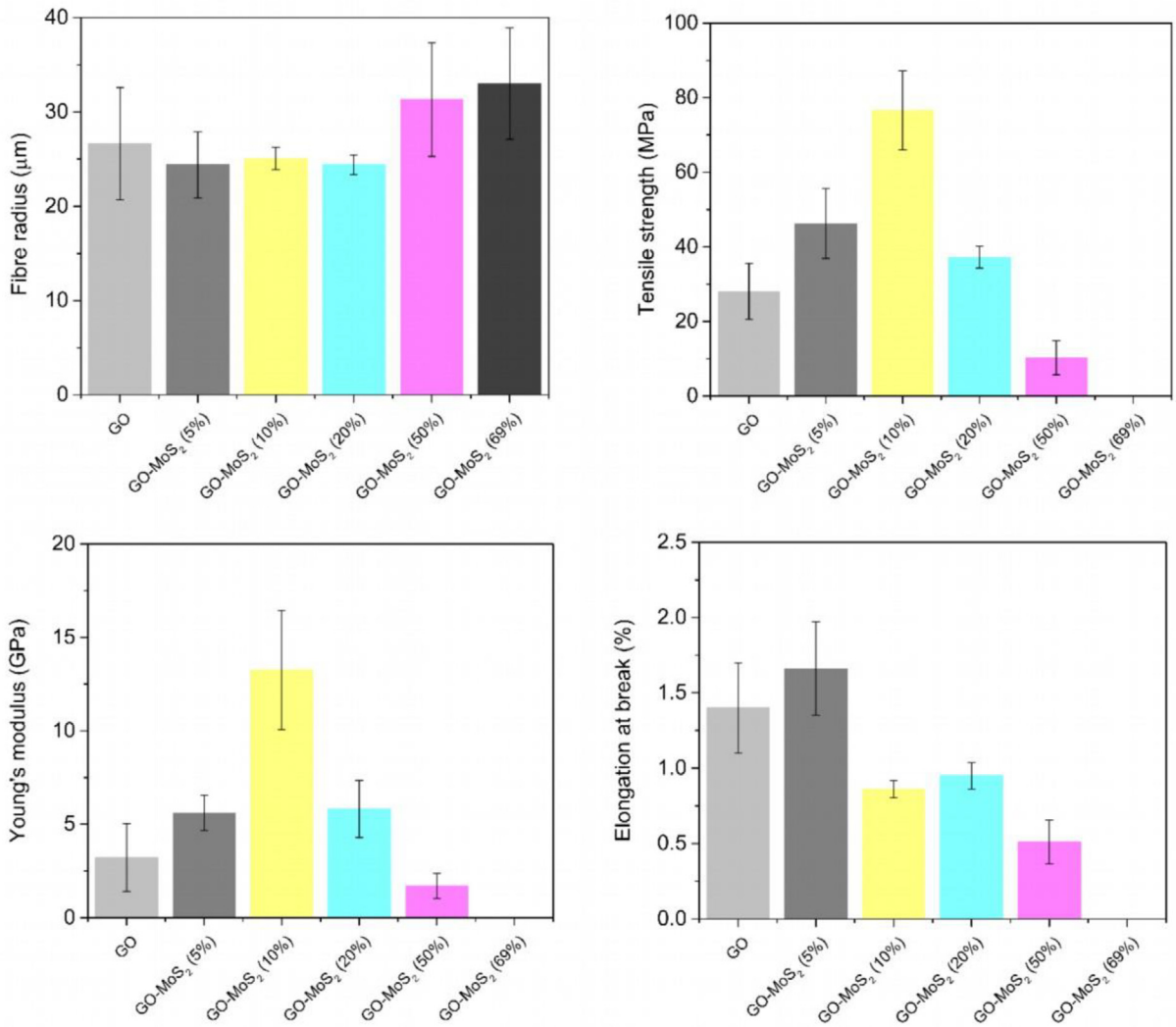

Fig. 6. Mechanical test results obtained from stress-strain curve showing (a) fibre radius, (b) tensile strength, (c) Young's modulus and (d) % elongation at break for GO and GO#MoS_2 composite fibres.

throughout the fibre were done via performing Raman spectrometry on number of individual spots in the composite fibres. The representative Raman spectra of GO#MoS_2 composite microfibres is shown in Fig. 4(d). The result shows a good correlation with the SEM micrographs as all the spectra consist of all the corresponding peaks for graphene oxide (GO) and exfoliated MoS_2.

XPS elemental analysis of GO-MoS_2 (10 wt.%) was conducted and the C/O ratios was calculated (Fig. S4). The atomic weight percentages of C1s and O1s were 77.29 wt.% and 18.74 wt.% respectively, and the C/O ratio was found to be 4.12. No peak for calcium was observed in full survey indicating the complete removal of $CaCl_2$.

XRD analysis was carried out to compare the spectra of pure MoS_2 nanosheets with 10 wt.% rGO-MoS_2 sample (Fig. S5 in SM). The results showed that during the liquid exfoliation with GO, the crystallinity of MoS_2 remain identical as all the identifying peaks of MoS_2 were seen in rGO-MoS_2 sample.

The thermal stability test using TGA (Fig. 5) of GO-MoS_2 composite fibres with different weight percentages of MoS_2 nanosheets were carried out to further confirm the MoS_2 loadings in the composites. The GO-MoS_2 composite fibres have seen to have an initial weight loss around 100 °C, which is attributed to the evaporation of surface absorbed water.

For the GO-MoS_2 composite fibres, the initial decomposition temperature of around 300 °C is attributed to the loss of co-intercalated water molecules and the liberation of co-intercalated citric acid. The weight loss in the temperature range of 300–700 °C is related to the oxidation of MoS_2 and the removal of organic molecules present in the composite fibres [54]. The highest residual weight at 700 °C was found for 69 wt% MoS_2 and decreased with the reduction of MoS_2 weight percentages.

The tensile properties of our neat GO and GO# MoS_2 wet spun fibres were carried out with DMA using the method described in the experimental section. Fig. S6 shows some typical load-displacement curves for GO and GO# MoS_2 composite fibres which are similar to the typical shapes reported in literature for this kind of fibres [34].

Fibre diameters and the results of the tensile properties obtained from the mechanical study of the fibres are presented in Fig. 6. The details of the calculation procedure of tensile strength, Young's modulus, and elongation at break is given in Appendix A of SM. The average fibre diameters are found to be about 27 μm for neat GO and 26 to 29 μm for GO# MoS_2 composite fibres at different MoS_2 content. However, the average fibre diameters of different fibres do not seem to be significantly different considering their standard deviations. From the results of the tensile properties, it can be seen that the tensile strength and Young's modulus was 28 MPa and 3.2 GPa, respectively for bare GO and they were found to increase with the increase of the content of MoS_2 up to 10 wt.%. The addition of MoS_2 beyond 10 wt.% (20 wt.% and 50 wt.% in

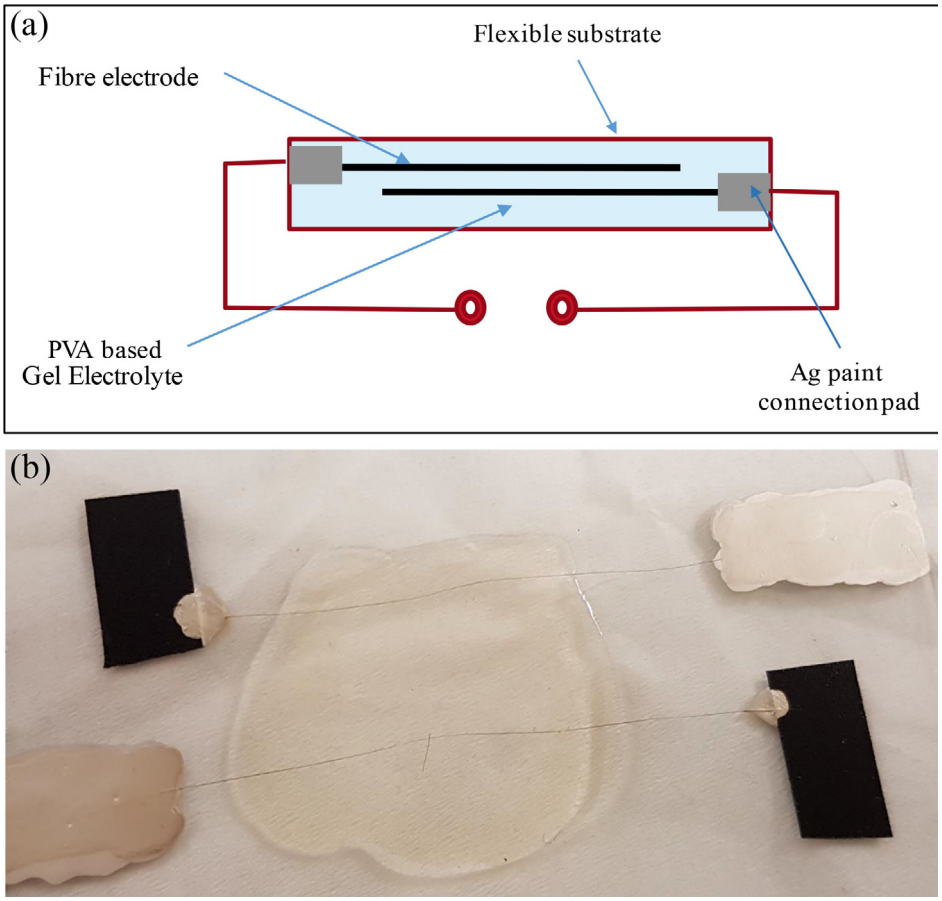

Fig. 7. (a) Schematic illustration of a two-electrode fibre supercapacitor device and (b) an actual device tested electrochemically made of two rGO-MoS_2 (20 wt%) fibre.

this case) was seen to reduce the tensile properties. Although fibre manufacturing using MoS_2 content of 69 wt.% was possible using the current method, the fibres were too weak to withstand the testing preload of 0.001 N. The highest tensile strength and Young's modulus (76.5 MPa and 13.3 GPa, respectively) was obtained for MoS_2 content of 10 wt.%. The best intermolecular interaction between GO and MoS_2 is believed to obtain at this fibre content to produce synergistic effect to increase the tensile properties. Above 10 wt.% MoS_2 content, (20 wt.%, 50 wt.% and 69 wt.% in this case) the fibre properties become MoS_2 dominant, and hence, the fibre becomes weak and eventually fails. Elongation at break (%) was found to increase for fibres with 5% MoS_2 content and was found to decrease for 10 wt.% MoS_2 content which would be expected as the Young's modulus was increased to a great extent for this type of fibres.

As a proof-of-concept application of the composite microfibres we fabricate two electrode solid state supercapacitor device and tested their performance using a potentiostat. The photograph and a schematic of the device is shown in Fig. 7.

The two-electrode configuration was tested using cyclic voltammetry and galvanostatic charge discharge in H_2SO_4 based polymer gel electrolyte. Well defined CV curves were observed within the potential window of 0.0 V to -0.8 V as can be seen in Fig. 8 (a–e). For all five devices, an increase in current density with the increase in scan rate is observed. A comparison of all the devices at 5 mV s^{-1} is shown in Fig. 8 (f). Comparatively higher current densities were observed per unit volume with increased loading of MoS_2 in the fibre up to 20 wt.% MoS_2 after when it decreased substantially. The CV curves of rGO fibre (Fig. 8a). showed the presence of pseudocapacitive behaviour and resistive in nature due to the low-conductivity of rGO.[55]. The addition of 5 wt.% MoS_2 in the rGO fibre showed the enhancement of the conductivity as well as improved electrical double layer capacitance (EDLC) behaviour (Fig. 8b). The further addition of MoS_2 (10, 20 & 50 wt.%) in the rGO fibres indicated their capacitive behaviour was more EDLC contributed (Fig. 8c). It is also worth noting the improvement in the shape of the CV curve with the addition of MoS_2 in the fibre. The improvement is believed to be due to efficient incorporation of MoS_2 particles between large GO sheets that act as nanospacer and prevents the restacking of the reduced GO layers. It also improves ion diffusion and charge transfer in the fibre electrodes [56,57].

The galvanostatic charge discharge curves for all the devices are shown in Fig. 9(a–c). The charge-discharge curves resemble typical triangular shape for different MoS_2 loadings with a slight potential drop. The volumetric capacitance was calculated from the discharge curves according to Eq 1, and the results are plotted against current densities as shown in Fig. 9(d). As can be seen here, with the increase in MoS_2 loading the volumetric capacitance starts to increase up to 20 wt% and above this MoS_2 content the volumetric capacitance starts to decrease rapidly. Firstly, with the increment of weight ratio of MoS_2 in rGO fibre, the MoS_2 may induce semiconducting environment in the fibre. It may obstruct the conductivity of the electrodes and thus decrease the capacitive properties. Secondly, the decrease in mechanical property may reduce the capacitance properties due to the poor mechanical connection in the fibres.

The highest volumetric capacitance of 55.4 F cm^{-3} (areal capacitance of 282.6 mF cm^{-2}) was observed for GO#MoS_2 (20 wt%) at current density of 2.3 mA cm^{-3} (Fig. 9(e)). Based on the charge-

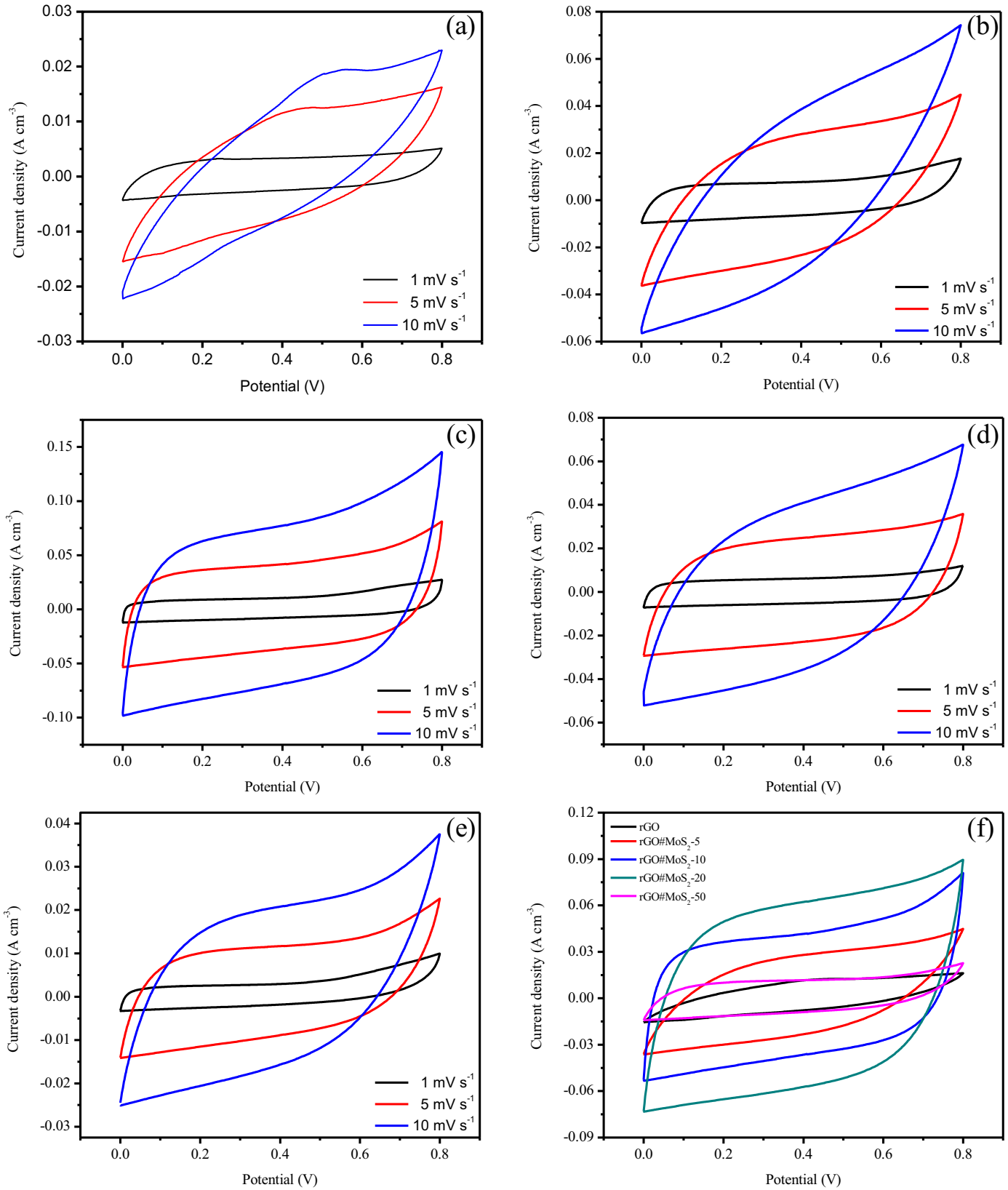

Fig. 8. Representative CV patterns of supercapacitor devices at different scan rate made of (a) rGO, (b) rGO-MoS_2 (5 wt%), (c) rGO-MoS_2 (10 wt%), (d) rGO-MoS_2 (20 wt%), (e) rGO-MoS_2 (50 wt%) in H_2SO_4–PVA gel electrolyte. (f) A comparison of CVs at 5 mV s^{-1} for all the capacitor devices.

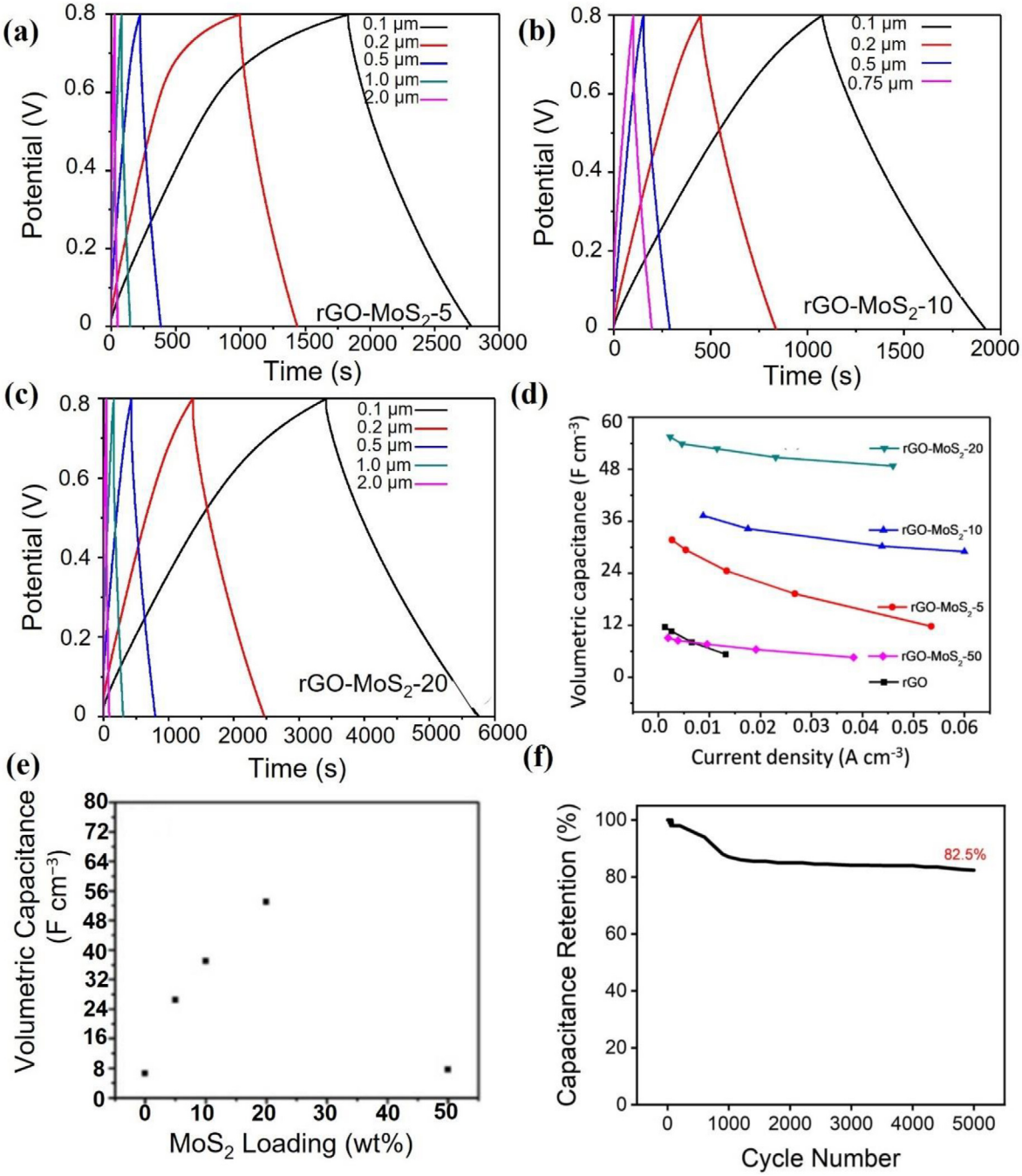

Fig. 9. Galvanostatic charge discharge curves of supercapacitor devices at different currents for (a) rGO-MoS_2 (5 wt%), (b) rGO-MoS_2 (10 wt%), (c) rGO-MoS_2 (20 wt%) in H_2SO_4–PVA gel electrolyte. (d) Comparison of device volumetric capacitance calculated from discharge curve for all the devices at different current densities, (e) Volumetric capacitance calculated from the charge-discharge study at 10 mA cm^{-3} current density plotted against MoS_2 loading in the composite fibres, and (f) capacity retention curve showing the cycling stability of rGO-MoS_2 (20 wt.%) fibre-based supercapacitor device at a current rate of 2.5 μA.

discharge result, we studied the cycling stability of GO#MoS_2 (20 wt%) device. The device shows good cycling stability with 82.5 % capacity retention after 5000 cycles as depicted in Fig. 9(f). The stable capacitance retention after 1200 cycles indicates that the initial drops of the overall capacitance was due to the contribution of the pseudocapacitance from the oxide groups and MoS_2. After certain cycles (∼ 1000 cycles) that pseudocapacitive contribution get reduced and the remaining stable capacitance is maintained by the intrinsic electrical double layer capacitance (EDLC).

Table 1 summarises the performances of some recently reported graphene and MoS_2 based fibre supercapacitors along with the performances of the fibre supercapacitors produced in the present study. The capacitance performances and cycle life of the fibre supercapacitors produced in the present study are comparable to those reported in the literature.

The results obtained from the electrochemical study suggest very high potential for the implementation of our technique to produce hybrid microfibres. These hybrid microfibres can be utilized as high efficiency flexible material to fabricate all solid-state cable capacitor that can be used in smart textile of the future. Moreover, this study shows the simple wet spinning strategy that can be extended to produce flexible hybrid microfibres by compositing any 2D layered material with GO.

4. Conclusions

We have presented an efficient, low cost, binder-free wet spinning approach to prepare composite microfibres. High MoS_2 loading of up to 69 wt.% in the GO#MoS_2 composite fibre was achieved by this method. Solid-state fibre supercapacitor devices were fabricated using these fibres and their performance was evaluated. The fibres demonstrated improved mechanical properties with addition of MoS_2 up to 10 wt.% after which the mechanical performance degradation was observed. Supercapacitor device fabricated with rGO#MoS_2 (20 wt.%) shows highest areal capacitance (282.6 mF cm^{-2}) with excellent cycling stability of 82.5 % after 5000 charge-discharge cycles. The results show a great promise for the reported wet spinning approach in fabricating composite fibres involving LC-GO and other 2D layered materials at ease. Even though the mechanical properties degraded after 10 wt.% and capacitance properties degraded after 20 wt.%, the possibilities of loading 69 wt.% of MoS_2 in rGO fibres reported in this work can open up several areas of applications on wearable electronics, fibrous sensors and printed electronics. The mechanical tests performed in the present study was to determine the tensile strength (fibre failure stress) of the fibres. As it was a destructive process, changing of capacitance with mechanical stress was not considered. However, to determine the capacitance change with fibre stress (before failure stress), there needs an extensive set of experiments which was out of scope of this study. In terms of checking capacitance trend with fibre surface area as reported by [63], effort was made to keep the diameter of the fibres similar by using a needle of constant diameter. To measure the change of capacitance with surface area, the diameter of the needle needed to be altered which would require a series of experiments. Again, it was out of the scope of this study. These two studies on fibrous energy storage are indeed interesting and therefore, further studies will be conducted to investigate the effect of stress on capacitance and to modify the surface area of the fibres by changing the fibre diameters with various needle widths used in the electro spinning process.

Declaration of Competing Interest

The authors declare that they have no known competing financial interests or personal relationships that could have appeared to influence the work reported in this paper.

Supplementary materials

Supplementary material associated with this article can be found, in the online version, at doi:10.1016/j.cartre.2021.100097.

References

[1] Y. Song, H. Chen, Z. Su, X. Chen, L. Miao, J. Zhang, X. Cheng, H. Zhang, Highly compressible integrated supercapacitor–piezoresistance-sensor system with CNT–PDMS sponge for health monitoring, Small 13 (39) (2017) 1702091.
[2] K. Cherenack, L. Van Pieterson, Smart textiles: challenges and opportunities, J. Appl. Phys. 112 (9) (2012) 091301.
[3] M. Chan, D. Estève, J.Y. Fourniols, C. Escriba, E. Campo, Smart wearable systems: current status and future challenges, Artif. Intell. Med. 56 (3) (2012) 137–156.
[4] A. Lymberis, S. Olsson, Intelligent biomedical clothing for personal health and disease management: state of the art and future vision, Telemed. J. e-health 9 (4) (2003) 379–386.
[5] K. Cherenack, C. Zysset, T. Kinkeldei, N. Münzenrieder, G. Tröster, Woven electronic fibers with sensing and display functions for smart textiles, Adv. Mater. 22 (45) (2010) 5178–5182.
[6] A. Schwarz-Pfeiffer, M. Hoerr, V. Mecnika, Textiles with integrated sleep-monitoring sensors, Adv. Smart Med. Text. Treat. Health Monit. (2015) 197.
[7] D. Yu, Q. Qian, L. Wei, W. Jiang, K. Goh, J. Wei, J. Zhang, Y. Chen, Emergence of fiber supercapacitors, Chem. Soc. Rev. 44 (3) (2015) 647–662.
[8] Y.H. Lee, J.S. Kim, J. Noh, I. Lee, H.J. Kim, S. Choi, J. Seo, S. Jeon, T.S. Kim, J.Y. Lee, J.W. Choi, Wearable textile battery rechargeable by solar energy, Nano Lett. 13 (11) (2013) 5753–5761.
[9] G. Sun, J. Liu, X. Zhang, X. Wang, H. Li, Y. Yu, W. Huang, H. Zhang, P. Chen, Fabrication of ultralong hybrid microfibers from nanosheets of reduced graphene oxide and transition-metal dichalcogenides and their application as supercapacitors, Angew. Chem. 126 (46) (2014) 12784–12788.
[10] G. Sun, X. Zhang, R. Lin, J. Yang, H. Zhang, P. Chen, Hybrid fibers made of molybdenum disulfide, reduced graphene oxide, and multi-walled carbon nanotubes for solid-state, flexible, asymmetric supercapacitors, Angew. Chem. Int. Ed. 54 (15) (2015) 4651–4656.
[11] B. Wang, Q. Wu, H. Sun, J. Zhang, J. Ren, Y. Luo, M. Wang, H. Peng, An intercalated graphene/(molybdenum disulfide) hybrid fiber for capacitive energy storage, J. Mater. Chem. A 5 (3) (2017) 925–930.
[12] W. Zhang, P. Zhang, Z. Su, G. Wei, Synthesis and sensor applications of MoS 2-based nanocomposites, Nanoscale 7 (44) (2015) 18364–18378.
[13] Y. Liu, G. Sun, C. Jiang, X.T. Zheng, L. Zheng, C.M. Li, Highly sensitive detection of hydrogen peroxide at a carbon nanotube fiber microelectrode coated with palladium nanoparticles, Microchim. Acta 181 (1-2) (2014) 63–70.
[14] J. Foroughi, G.M. Spinks, G.G. Wallace, J. Oh, M.E. Kozlov, S. Fang, T. Mirfakhrai, J.D. Madden, M.K. Shin, S.J. Kim, Torsional carbon nanotube artificial muscles, Science 334 (6055) (2011) 494–497.
[15] M.D. Lima, N. Li, M.J. De Andrade, S. Fang, J. Oh, G.M. Spinks, M.E. Kozlov, C.S. Haines, D. Suh, J. Foroughi, Electrically, chemically, and photonically powered torsional and tensile actuation of hybrid carbon nanotube yarn muscles, Science 338 (6109) (2012) 928–932.
[16] M.R. Lee, R.D. Eckert, K. Forberich, G. Dennler, C.J. Brabec, R.A. Gaudiana, Solar power wires based on organic photovoltaic materials, Science 324 (5924) (2009) 232–235.
[17] B. Weintraub, Y. Wei, Z.L. Wang, Optical fiber/nanowire hybrid structures for efficient three-dimensional dye-sensitized solar cells, Angew. Chem. 121 (47) (2009) 9143–9147.
[18] S. Pan, Z. Yang, P. Chen, J. Deng, H. Li, H. Peng, Wearable solar cells by stacking textile electrodes, Angew. Chem. Int. Ed. 53 (24) (2014) 6110–6114.
[19] W. Weng, Q. Sun, Y. Zhang, H. Lin, J. Ren, X. Lu, M. Wang, H. Peng, Winding aligned carbon nanotube composite yarns into coaxial fiber full batteries with high performances, Nano Lett. 14 (6) (2014) 3432–3438.
[20] A. Reina, X. Jia, J. Ho, D. Nezich, H. Son, V. Bulovic, M.S. Dresselhaus, J. Kong, Large area, few-layer graphene films on arbitrary substrates by chemical vapor deposition, Nano Lett. 9 (1) (2008) 30–35.
[21] R. Mas-Balleste, C. Gomez-Navarro, J. Gomez-Herrero, F. Zamora, 2D materials: to graphene and beyond, Nanoscale 3 (1) (2011) 20–30.
[22] S. Park, R.S. Ruoff, Chemical methods for the production of graphenes, Nat. Nanotechnol. 4 (4) (2009) 217–224.
[23] Y. Sun, Q. Wu, G. Shi, Graphene based new energy materials, Energy Environ. Sci. 4 (4) (2011) 1113–1132.
[24] K.S. Novoselov, V.I. Falko, L. Colombo, P.R. Gellert, M.G. Schwab, K. Kim, A roadmap for graphene, Nature 490 (7419) (2012) 192–200.
[25] A.K. Geim, Graphene: status and prospects, Science 324 (5934) (2009) 1530–1534.
[26] A.K. Geim, K.S. Novoselov, The rise of graphene, Nat. Mater. 6 (3) (2007) 183–191.
[27] S.H. Aboutalebi, R. Jalili, D. Esrafilzadeh, M. Salari, Z. Gholamvand, S. Aminorroaya Yamini, K. Konstantinov, R.L. Shepherd, J. Chen, S.E. Moulton, High-performance multifunctional graphene yarns: toward wearable all-carbon energy storage textiles, ACS Nano 8 (3) (2014) 2456–2466.
[28] X. Wang, G. Shi, Flexible graphene devices related to energy conversion and storage, Energy Environ. Sci. 8 (3) (2015) 790–823.
[29] Z. Xu, C. Gao, Graphene in macroscopic order: liquid crystals and wet-spun fibers, Acc. Chem. Res. 47 (4) (2014) 1267–1276.
[30] F. Meng, W. Lu, Q. Li, J.H. Byun, Y. Oh, T.W. Chou, Graphene-based fibers: a review, Adv. Mater. 27 (35) (2015) 5113–5131.
[31] Y. Meng, Y. Zhao, C. Hu, H. Cheng, Y. Hu, Z. Zhang, G. Shi, L. Qu, All-graphene core-sheath microfibers for all-solid-state, stretchable fibriform supercapacitors and wearable electronic textiles, Adv. Mater. 25 (16) (2013) 2326–2331.
[32] Q. Meng, H. Wu, Y. Meng, K. Xie, Z. Wei, Z. Guo, High-performance all-carbon yarn micro-supercapacitor for an integrated energy system, Adv. Mater. 26 (24) (2014) 4100–4106.
[33] R. Jalili, S.H. Aboutalebi, D. Esrafilzadeh, R.L. Shepherd, J. Chen, S. Aminorroaya-Yamini, K. Konstantinov, A.I. Minett, J.M. Razal, G.G. Wallace, Scalable one-step wet-spinning of graphene fibers and yarns from liquid crystalline dispersions of graphene oxide: towards multifunctional textiles, Adv. Funct. Mater. 23 (43) (2013) 5345–5354.
[34] S. Seyedin, M.S. Romano, A.I. Minett, J.M. Razal, Towards the knittability of graphene oxide fibres, Sci. Rep. 5 (2015) 14946.
[35] R. Jalili, S.H. Aboutalebi, D. Esrafilzadeh, K. Konstantinov, J.M. Razal, S.E. Moulton, G.G. Wallace, Formation and processability of liquid crystalline dispersions of graphene oxide, Mater. Horiz. 1 (1) (2014) 87–91.
[36] Y. Li, K. Sheng, W. Yuan, G. Shi, A high-performance flexible fibre-shaped electrochemical capacitor based on electrochemically reduced graphene oxide, Chem. Commun. 49 (3) (2013) 291–293.
[37] S.Z. Butler, S.M. Hollen, L. Cao, Y. Cui, J.A. Gupta, H.R. Gutiérrez, T.F. Heinz, S.S. Hong, J. Huang, A.F., Ismach, progress, challenges, and opportunities in two-dimensional materials beyond graphene, ACS Nano 7 (4) (2013) 2898–2926.
[38] Q.H. Wang, K. Kalantar-Zadeh, A. Kis, J.N. Coleman, M.S. Strano, Electronics and optoelectronics of two-dimensional transition metal dichalcogenides, Nat. Nano. 7 (11) (2012) 699–712.

[39] S.V.P. Vattikuti, P.C. Nagajyothi, K.C. Devarayapalli, J. Shim, Depositing reduced graphene oxide onto tungsten disulfide nanosheets via microwave irradiation: confirmation of four-electron transfer-assisted oxygen reduction and methanol oxidation reaction, New J. Chem. 44 (25) (2020) 10638–10647.
[40] H.H. Chien, K.J. Ma, S.P. Vattikuti, C.H. Kuo, C.B. Huo, C.L. Chao, Tribological behaviour of MoS2/Au coatings, Thin Solid Films 518 (24) (2010) 7532–7534.
[41] S.P. Vattikuti, P. Nagajyothi, K. Devarayapalli, K. Yoo, N.D. Nam, J. Shim, Hybrid Ag/MoS2 nanosheets for efficient electrocatalytic oxygen reduction, Appl. Surf. Sci. 526 (2020) 146751.
[42] P. Nagajyothi, K. Devarayapalli, J. Shim, S.P. Vattikuti, Highly efficient white-LED-light-driven photocatalytic hydrogen production using highly crystalline ZnFe2O4/MoS2 nanocomposites, Int. J. Hydrog. Energy 45 (57) (2020) 32756–32769.
[43] N. Joseph, P.M. Shafi, A.C. Bose, Recent advances in 2D-MoS_2 and its composite nanostructures for supercapacitor electrode application, Energy Fuels 34 (6) (2020) 6558–6597.
[44] K. Krishnamoorthy, P. Pazhamalai, G.K. Veerasubramani, S.J. Kim, Mechanically delaminated few layered MoS_2 nanosheets based high performance wire type solid-state symmetric supercapacitors, J. Power Sour. 321 (2016) 112–119.
[45] Y. Luo, Y. Zhang, Y. Zhao, X. Fang, J. Ren, W. Weng, Y. Jiang, H. Sun, B. Wang, X. Cheng, Aligned carbon nanotube/molybdenum disulfide hybrids for effective fibrous supercapacitors and lithium ion batteries, J. Mater. Chem. A 3 (34) (2015) 17553–17557.
[46] K.E. Lee, S.P. Sasikala, H.J. Lee, G.Y. Lee, S.H. Koo, T. Yun, H.J. Jung, I. Kim, S.O. Kim, Amorphous molybdenum sulfide deposited graphene liquid crystalline fiber for hydrogen evolution reaction catalysis, Part. Part. Syst. Charact. 34 (9) (2017) 1600375.
[47] S.H. Aboutalebi, M.M. Gudarzi, Q.B. Zheng, J.K. Kim, Spontaneous formation of liquid crystals in ultralarge graphene oxide dispersions, Adv. Funct. Mater. 21 (15) (2011) 2978–2988.
[48] J.N. Coleman, M. Lotya, A. O'Neill, S.D. Bergin, P.J. King, U. Khan, K. Young, A. Gaucher, S. De, R.J. Smith, I.V. Shvets, S.K. Arora, G. Stanton, H.Y. Kim, K. Lee, G.T. Kim, G.S. Duesberg, T. Hallam, J.J. Boland, J.J. Wang, J.F. Donegan, J.C. Grunlan, G. Moriarty, A. Shmeliov, R.J. Nicholls, J.M. Perkins, E.M. Grieveson, K. Theuwissen, D.W. McComb, P.D. Nellist, V. Nicolosi, Two-dimensional nanosheets produced by liquid exfoliation of layered materials, Science 331 (6017) (2011) 568–571.
[49] R. Kaindl, B.C. Bayer, R. Resel, T. Müller, V. Skakalova, G. Habler, R. Abart, A.S. Cherevan, D. Eder, M. Blatter, F. Fischer, J.C. Meyer, D.K. Polyushkin, W. Waldhauser, Growth, structure and stability of sputter-deposited MoS(2) thin films, Beilstein J. Nanotechnol. 8 (2017) 1115–1126.
[50] J. Wang, L. Shen, P. Nie, X. Yun, Y. Xu, H. Dou, X. Zhang, N-doped carbon foam based three-dimensional electrode architectures and asymmetric supercapacitors, J. Mater. Chem. A 3 (6) (2015) 2853–2860.
[51] J.E. Kim, T.H. Han, S.H. Lee, J.Y. Kim, C.W. Ahn, J.M. Yun, S.O. Kim, Graphene oxide liquid crystals, Angew. Chem. Int. Ed. 50 (13) (2011) 3043–3047.
[52] L. Onsager, The effects of shape on the interaction of colloidal particles, Ann. N. Y. Acad. Sci. 51 (4) (1949) 627–659.
[53] Z. Dong, C. Jiang, H. Cheng, Y. Zhao, G. Shi, L. Jiang, L. Qu, Facile fabrication of light, flexible and multifunctional graphene fibers, Adv. Mater. 24 (14) (2012) 1856–1861.
[54] R. Thangappan, S. Kalaiselvam, A. Elayaperumal, R. Jayavel, M. Arivanandhan, R. Karthikeyan, Y. Hayakawa, Graphene decorated with MoS 2 nanosheets: a synergetic energy storage composite electrode for supercapacitor applications, Dalton Trans. 45 (6) (2016) 2637–2646.
[55] K.K. Upadhyay, T. Nguyen, T.M. Silva, M.J. Carmezim, M. Montemor, Pseudocapacitive response of hydrothermally grown MoS_2 crumpled nanosheet on carbon fiber, Mater. Chem. Phys. 216 (2018) 413–420.
[56] J. Wang, Z. Wu, K. Hu, X. Chen, H. Yin, High conductivity graphene-like MoS2/polyaniline nanocomposites and its application in supercapacitor, J. Alloys Compd. 619 (2015) 38–43.
[57] M.A. Bissett, I.A. Kinloch, R.A. Dryfe, Characterization of MoS2–graphene composites for high-performance coin cell supercapacitors, ACS Appl. Mater. Interfaces 7 (31) (2015) 17388–17398.
[58] L. Liu, Y. Yu, C. Yan, K. Li, Z. Zheng, Wearable energy-dense and power-dense supercapacitor yarns enabled by scalable graphene–metallic textile composite electrodes, Nat. Commun. 6 (1) (2015) 1–9.
[59] Y. Cao, M. Zhu, P. Li, R. Zhang, X. Li, Q. Gong, K. Wang, M. Zhong, D. Wu, F. Lin, Boosting supercapacitor performance of carbon fibres using electrochemically reduced graphene oxide additives, Phys. Chem. Chem. Phys. 15 (45) (2013) 19550–19556.
[60] Y. Hu, H. Cheng, F. Zhao, N. Chen, L. Jiang, Z. Feng, L. Qu, All-in-one graphene fiber supercapacitor, Nanoscale 6 (12) (2014) 6448–6451.
[61] J. Li, Y. Shao, P. Jiang, Q. Zhang, C. Hou, Y. Li, H. Wang, 1T-Molybdenum disulfide/reduced graphene oxide hybrid fibers as high strength fibrous electrodes for wearable energy storage, J. Mater. Chem. A 7 (7) (2019) 3143–3149.
[62] X. Jian, H. Li, H. Li, Y. Li, Y. Shang, Flexible and freestanding MoS2/rGO/CNT hybrid fibers for high-capacity all-solid supercapacitors, Carbon 172 (2021) 132–137.
[63] A. Pedico, A. Lamberti, A. Gigot, M. Fontana, F. Bella, P. Rivolo, M. Cocuzza, C.F. Pirri, High-performing and stable wearable supercapacitor exploiting rGO aerogel decorated with copper and molybdenum sulfides on carbon fibers, ACS Appl. Energy Mater. 1 (9) (2018) 4440–4447.